The nature of the multi-wavelength emission of 3C 111

S. de Jong, V. Beckmann, and F. Mattana

François Arago Centre, APC, Université Paris Diderot, CNRS/IN2P3, CEA/Irfu, Observatoire de Paris, Sorbonne Paris Cité,
10 rue Alice Domon et Léonie Duquet, 75205 Paris Cedex 13, France
e-mail: dejong@in2p3.fr

ABSTRACT

Aims. We attempt to determine the nature of the high energy emission of the radio galaxy 3C 111, by distinguishing between the effects of the thermal and non-thermal processes.
Methods. We study the X-ray spectrum of 3C 111 between 0.4 keV and 200 keV, and its spectral energy distribution, using data from the *Suzaku* satellite combined with INTEGRAL, *Swift*/BAT data, and *Fermi*/LAT data. We then model the overall spectral energy distribution by including radio and infrared data.
Results. The combined *Suzaku*, *Swift* and INTEGRAL data are represented by an absorbed exponentially cut-off power-law with reflection from neutral material with a photon index $\Gamma = 1.68 \pm 0.03$, a high-energy cut-off $E_{\mathrm{cut}} = 227^{+143}_{-67}$ keV, a reflection component with $R = 0.7 \pm 0.3$ and a Gaussian component to account for the iron emission-line at 6.4 keV with an equivalent width of $EW = 85 \pm 11$ eV. The X-ray spectrum appears dominated by thermal, Seyfert-like processes, but there are also indications of non-thermal processes. The radio to γ-ray spectral energy distribution can be fit with a single-zone synchrotron-self Compton model, with no need for an additional thermal component.
Conclusions. We suggest a hybrid scenario to explain the broad-band emission, including a thermal component (iron line, reflection) that dominates in the X-ray regime and a non-thermal one to explain the spectral energy distribution.

Key words. galaxies: active – gamma rays: galaxies – X-rays: galaxies – galaxies: individual: 3C 111

1. Introduction

Radio galaxies are a subclass of active galactic nuclei (AGNs) and in the unification model of AGN radio galaxies are the radio-loud counterparts of Seyfert galaxies (Antonucci 1993; Urry & Padovani 1995). For both of these classes, it is thought that the inclination is large, such that the observer views the core, which is dominated by thermal processes through absorbing material. This differs from blazars, where the inclination angle is very small. The observed emission originates in the relativistic jet, which is dominated by non-thermal processes. Owing to the Doppler boosting of the emission in the jet, the energy of the observed emission from blazars can reach the γ-ray regime, even up to TeV energies. Several non-blazar AGNs have also been found to emit significantly in the γ-ray regime (Hartman et al. 2008; Abdo et al. 2010c; Ackermann et al. 2011). Although there have been several theories (i.e. misaligned jet, shocks in the radio lobes) about the origin of this high-energy radiation, conclusive support of any of these theories is yet to be found.

3C 111 is a nearby ($z = 0.049$, Sargent 1977) flat-spectrum FR-II radio galaxy (Fanaroff & Riley 1974; Linfield & Perley 1984) that displays strong, broad emission-lines in the optical (Sargent 1977) and an iron-emission line in the X-ray regime (Lewis et al. 2005), similar to Seyfert galaxies. In the radio regime, the galaxy's emission is dominated by the relativistic jet, which has an angle of 18° to our line of sight (Jorstad et al. 2005). The projected size of the jet is 78 kpc (Bridle & Perley 1984). There is no visible counter-jet, although a bright lobe is detectable in the opposite direction of the observed jet, which is likely fed by the undetected counter-jet (Linfield & Perley 1984).

Earlier studies of 3C 111 in the X-ray band have identified the high energy cut-off of the spectrum. Dadina (2007) found a lower limit of $E_{\mathrm{cut}} \geq 82$ keV using *BeppoSAX* data and Ballo et al. (2011) derived a similar lower limit to the cut-off of $E_{\mathrm{cut}} \geq 75$ keV, using data from *XMM-Newton* and *Suzaku*/XIS and PIN. Molina et al. (2009), using *XMM-Newton*, *Swift*, and INTEGRAL data, constrained the cut-off energy to be $E_{\mathrm{cut}} = 126^{+193}_{-50}$ keV. It is uncertain whether a reflection component is present in the X-ray spectrum. An upper limit of $R \leq 2.25$ was found by Dadina (2007) using *BeppoSAX* data and constraints of $R = 0.9 \pm 0.6$ were derived by Molina et al. (2009) and $R = 0.35 \pm 0.06$ by Ballo et al. (2011) using *Suzaku*/XIS and PIN data. Ballo et al. (2011) used *XMM-Newton* data to find the reflection in the energy range 0.4–10 keV to be $R = 0.19^{+0.05}_{-0.04}$. Rivers et al. (2011) did not detect a reflection component, using RXTE data between 3 keV and $\gtrsim$100 keV. The equivalent width (EW) of the iron line at 6.1 keV has been measured several times and is likely variable. Ballo et al. (2011) and Tombesi et al. (2010) found similar values of $EW = 75 \pm 13$ eV (*Suzaku*/XIS and PIN) and $EW = 86 \pm 16$ eV (*Suzaku*/XIS), respectively. Using *Suzaku*/XIS data of three different observations taken two years later, Tombesi et al. (2011) found a smaller EW of between $EW > 33$ eV and $EW > 40$ eV. Similarly, Ballo et al. (2011) used *XMM-Newton* data to fit the 0.4–10 keV spectrum and found an $EW = 38^{+11}_{-9}$ eV.

3C 111 has been detected in γ-rays by CGRO/EGRET (Hartman et al. 1999; Sguera et al. 2005; Hartman et al. 2008), and was included in the first *Fermi*/LAT catalogue (Abdo et al. 2010a). In the second *Fermi*/LAT catalogue, the source was omitted since it had no longer been significantly detected

(Nolan et al. 2012). 3C 111 is likely variable in the γ-ray regime (Ackermann et al. 2011). Using 24 months of *Fermi*/LAT data, Grandi et al. (2012) found 3C 111 to be detectable during a short time-period ($\Delta t \sim 30{-}60$ days), limiting the radius of the emission region to be $R < 0.1$ pc (assuming a Doppler factor of $\delta = 3$) based on causality arguments. The detectability of the source in the GeV energy range coincided with an increase in the flux in the millimeter, optical and X-rays regimes, indicating the emission is likely to emerge from the same region. Since the outburst in millimeter, optical, and X-rays is associated with the ejection of a bright radio knot, this indicates that the GeV emission originates from the radio core within 0.3 pc of the central supermassive black hole.

To understand the physical processes causing the emission in 3C 111, we first study the X-ray to γ-ray spectrum to find whether the emission is the product of thermal (Seyfert-like) or non-thermal processes (blazar-like) or a combination of both. We then model the spectral energy distribution (SED) to understand the processes dominating the broad-band radiation of 3C 111 from radio to high energies.

2. Observations and data reduction

To cover a large energy band from X-rays to γ-rays and study the high-energy emission from 3C 111, we used data from several different instruments.

2.1. Suzaku-XIS/PIN

3C 111 was observed by *Suzaku* from 22 August 2008 to 25 August 2008 with a total elapsed time of 236.9 ks in HXD nominal pointing mode. We analysed data from the X-ray Imaging Spectrometer (XIS, Koyama et al. 2007) and Hard X-ray Detector (HXD, Takahashi et al. 2007). The XIS instrument consists of three separate CCD detectors and has an energy range of $\sim$0.2–12.0 keV. The HXD is a collimated instrument, consisting of two independent detector systems, silicon PIN diodes that function in the range $\sim$10–60 keV and GSO scintillation counters covering the energy range $\sim$30–600 keV.

For the observations made with the XIS, we used the clean events provided by the instrument team where the standard event cuts had been applied.

The flux of 3C 111 is too low above 70 keV to extract a significant spectrum from the HXD/GSO detector, hence we used only HXD/PIN data. The *Suzaku* team provides a response file for the PIN, which depends on both the epoch in which the data were taken and the pointing mode. In addition a non X-ray background (NXB) per observation is available for the PIN analysis. After filtering the source and background files in time using the good time intervals, we extracted the source and background spectra. The source spectrum needed to be corrected for dead-time events, which we achieved using HXDDTCOR. The NXB was simulated with ten times more counts to suppress statistical errors. We therefore needed to increase the exposure time of the background spectrum by a factor of ten. Using XSPEC, we simulated the cosmic X-ray background (CXB) using the PIN response file for the flat emission distribution in the proper epoch and point mode. We combined the NXB and CXB files and used this as a background in our analysis.

2.2. INTEGRAL IBIS/ISGRI

The International Gamma-Ray Astrophysics Laboratory (INTEGRAL; Winkler et al. 2003) is a γ-ray observatory with several instruments on board. We used the INTEGRAL Soft Gamma-Ray Imager (ISGRI), which is part of the Imager on Board INTEGRAL Spacecraft (IBIS), a coded-mask detector. ISGRI is sensitive between 15 keV to 1 MeV (Lebrun et al. 2003).

We used all data collected by INTEGRAL since the launch of the satellite up to August 2009, with a total exposure time of 508 ks. We first created individual spectra for all science windows (a science window is all data produced during one pointing) using the IBIS_SCIENCE_ANALYSIS routine. We then summed all the individual spectra to achieve a higher signal-to-noise ratio.

2.3. Swift-BAT

The Burst Alert Telescope (BAT) aboard the *Swift* satellite is a coded-aperture camera with an energy range of 14–195 keV for imaging (Barthelmy et al. 2005). Since the BAT telescope monitors the sky continuously and has a large field of view (1.4 sr, partially coded), it has regularly observed 3C 111.

We used data from the 58-month hard X-ray survey, from 2004 December to the end of 2009 May (see Tueller et al. 2010; Baumgartner et al. 2010). The detected flux for 3C 111 in this survey is 1.2×10^{-10} erg cm^{-2} s^{-1} between 14 keV and 195 keV.

2.4. Fermi-LAT

The Large Area Telescope (LAT) aboard the *Fermi* satellite operates in an energy range between 20 MeV and 300 GeV (Atwood et al. 2009). The LAT is a pair-conversion telescope with a very wide field of view that scans the sky continuously. During the nominal all-sky survey observing mode of *Fermi*/LAT, a total effective exposure time of 83.7 Ms was accumulated in the direction of 3C 111 between 4 August 2008 and 20 April 2011.

We selected diffuse-event-class photons (P6_V3 instrument response functions) between 100 MeV and 200 GeV in a circular region of interest with radius of 15° around the source. Events with a zenith angle of more than 105° were excluded (Abdo et al. 2009). We used the standard cuts proposed by the *Fermi* team based on the data quality of the events and the instrument configuration.

The maximum-likelihood analysis tool GTLIKE models all the emission in a given region, which can contain several sources. The goodness of fit is expressed as the log-likelihood value which is the probability of obtaining the data given an input model. After creating a model including all detectable sources in the field, we used GTLIKE to fit the model until the log-likelihood value was maximised. We found the test statistic value of 3C 111 to be $TS = 12.8$, which corresponds to a significance of $\sim 3\sigma$. The data provided only two significant points so it is impossible to fit the spectrum in e.g. XSPEC. However, when creating the spectrum, GTLIKE gives a spectral slope of $\Gamma_\gamma = 2.41 \pm 0.17$ across the range 0.1–200 GeV and a flux of $f = 1.2 \times 10^{-8}$ ph cm^{-2} s^{-1}.

3. Results

3.1. X-ray spectrum

We simultaneously fitted the X-ray spectra between 0.4 keV and 200 keV, in XSPEC (Arnaud 1996). We started our analysis by fitting the spectrum with an absorbed power-law and a

Table 1. Parameters for the individual power-law fits of the data, and their 90% confidence levels.

| Instrument	Epoch	Exposure time	PL index	f [erg cm^{-2} s^{-1}]	Energy range
XIS0	22–25 August 2008	95.4 ks	1.60 ± 0.02	$(2.20 \pm 0.02) \times 10^{-11}$	0.4–10 keV
XIS1	22–25 August 2008	95.4 ks	1.59 ± 0.02	$(2.24^{+0.03}_{-0.02}) \times 10^{-11}$	0.4–10 keV
XIS3	22–25 August 2008	95.4 ks	1.63 ± 0.02	$(2.2 \pm 0.02) \times 10^{-11}$	0.4–10 keV
PIN	22–25 August 2008	101.9 ks	1.52 ± 0.14	$(4.8 \pm 0.4) \times 10^{-11}$	12–60 keV
ISGRI	24 March 2003–19 August 2009	508 ks	1.90 ± 0.20	$(1.2 \pm 0.2) \times 10^{-10}$	20–200 keV
BAT	December 2004–May 2009	54 months[a]	1.99 ± 0.09	$(1.05 \pm 0.05) \times 10^{-10}$	15–150 keV
LAT	4 August 2008–20 April 2011	83.7 Ms	2.4 ± 0.2	$(6 \pm 2) \times 10^{-12}$	>100 MeV

Notes. [a] Elapsed time.
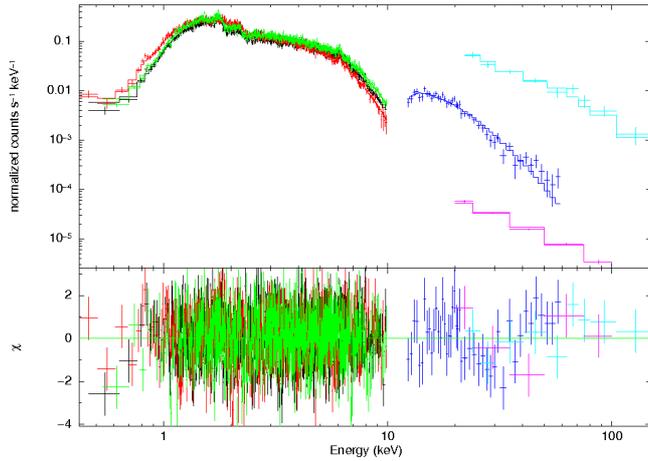
Fig. 1. Count spectrum of the combined *Suzaku*/XIS (0.4–10 keV), *Suzaku*/PIN (12–60 keV), INTEGRAL ISGRI (20–200 keV), and *Swift*/BAT (15–150) data with the fitted model: an absorbed cut-off power-law with reflection from neutral material and a Gaussian component to account for the iron line at 6.4 keV. The bottom panel shows the residuals in terms of the standard deviation with error bars of size one sigma.

Gaussian component at 6.1 keV to account for the redshifted iron emission-line. The fit resulted in a reduced chi-squared of $\chi^2_\nu = 1.14$ (1678 d.o.f.). We tried to improve our fit by using a cut-off power-law, which yielded a better fit with $\chi^2_\nu = 1.12$ (1677 d.o.f.). We explored the possibility of a broken power-law, but with a $\chi^2_\nu = 1.14$ (1676 d.o.f.), this gave no improvement in the fit. Adding a reflection component did further improve the fit, $\chi^2_\nu = 1.10$ (1676 d.o.f., F-test probability 4×10^{-8}). The resulting fit and the residuals are shown in Fig. 1. We derived the following best-fit parameters and 90% errors: the value for the equivalent hydrogen column-density $N_{\rm H} = (9.0 \pm 0.2) \times 10^{21}$ cm^{-2}, a power-law index of $\Gamma = 1.68 \pm 0.03$, a high-energy cut-off $E_{\rm cut} = 227^{+143}_{-67}$ keV and a reflection scaling factor of $R = 0.7 \pm 0.3$. Figure 2 shows the confidence contours of the reflection component versus the cut-off energy with $\Delta\chi^2$ of 68%, 90%, and 99.7%. We can exclude a cut-off below 130 keV at the 99.7% confidence level.

We fitted the data with a more physical model, `compPS` (Poutanen & Svensson 1996), which describes the process of thermal Comptonization. In this model, seed photons from the cool, thick accretion disc are injected into the electron plasma. The electron cloud can have several geometries, and we chose a plane-parallel slab: we also applied other geometries but found that they neither influenced the parameter values nor improved the fit. The electrons in the cloud have a Maxwellian distribution
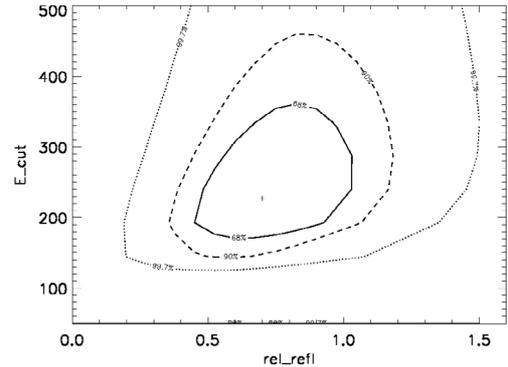

Fig. 2. Error contours for the best-fit `pexrav` model, reflection component R vs. the high-energy cut-off $E_{\rm cut}$. The contour levels correspond to $\Delta\chi^2$ of the 68%, 90%, and 99.7% statistical confidence regions. A cut-off below 130 keV is excluded at a 99.7% level.

with an electron temperature $T_{\rm e}$ and an optical depth τ related to the Compton parameter $y = 4\tau k T_{\rm e}/(m_{\rm e} c^2)$. The seed photons are up-scattered from their initial energy $E_{\rm i}$ to $E_{\rm f} = e^y E_{\rm i}$. The Compton scattering of the seed photons with the electrons in the plasma results in a spectrum that is afterwards reflected from a cool medium and then smeared out by the rotation of the disc.

The best-fit model gave a $\chi^2_\nu = 1.10$ (1676 d.o.f.). The values that we found for this model are an equivalent hydrogen column-density $N_{\rm H} = (9.0 \pm 0.2) \times 10^{21}$ cm^{-2}, a temperature of the electrons $k T_{\rm e} = 91^{+22}_{-48}$ keV, a reflection component $R = 1.8^{+0.5}_{-0.7}$, and a Compton parameter of $y = 0.6 \pm 0.1$, which corresponds to an optical depth $\tau = 0.8$.

We also fitted all data sets individually with an absorbed power-law and a Gaussian component. The values of the flux levels and power-law indices for these individual best fits to the data can be found in Table 1.

The measurements of the iron line at 6.4 keV are consistent in all three *Suzaku*/XIS spectra. After adding the three spectra together, we derived a line energy $E_{\rm line} = 6.11 \pm 0.02$ keV and an $EW = 85 \pm 11$ eV.

3.2. Fitting of the time-averaged SED

After we had created a SED based on our data, we modelled it with a public synchrotron self-Compton (SSC) code developed by Krawczynski et al. (2004)[1]. The SSC mechanism assumes an isotropic population of high-energy electrons that emit synchrotron radiation followed by inverse Compton scattering of the

---

[1] http://jelley.wustl.edu/multiwave/spectrum/?code

Table 2. Parameters used to model the SED of 3C 111 using the code by Krawczynski et al. (2004).

Symbol	Description	3C 111	Cen A	Mrk 421
δ	Doppler factor	14	1.0	10.0
$R_{\rm s}$	Radius of the emission volume [cm]	2×10^{16}	3.0×10^{15}	7.0×10^{15}
B	Magnetic field of emission volume [G]	4×10^{-2}	6.2	0.405
$E_{\rm min}$	Minimum energy of the electron distribution [eV]	5.6×10^{6}	1.5×10^{8}	3.2×10^{6}
$E_{\rm max}$	Maximum energy of the electron distribution [eV]	6.8×10^{9}	5.0×10^{13}	1.7×10^{11}
$E_{\rm br}$	Break energy of the electron distribution [eV]	–	4.0×10^{8}	2.2×10^{10}
p_1	Spectral index of electron spectrum ($E_{\rm min}$ to $E_{\rm br}$)	2	1.8	2.05
p_2	Spectral index of electron spectrum ($E_{\rm br}$ to $E_{\rm max}$)	–	4.3	3.6
$\log L$	Bolometric luminosity (3–200 keV) [erg s^{-1}]	44.7	42.5[a]	45.5[b]

Notes. For comparison, we include the fit parameters for the core of Centaurus A (Abdo et al. 2010b) and Markarian 421 (low flux state, Błażejowski et al. 2005). [a] Beckmann et al. (2011); [b] Lichti et al. (2008)

synchrotron photons to higher energies (Maraschi et al. 1992). The inverse Compton component may also include a thermal component of external seed photons (e.g. from the broad-line region or accretion disc) that are also Compton upscattered to high energies (external Compton component, Dermer & Schlickeiser 1993). The electron population is located in a spherical volume of radius $R_{\rm s}$ with a randomly oriented magnetic field B that moves relativistically towards the observer with a bulk Lorentz factor of Γ and an angle between the jet and the line of sight of θ. Thus, the radiation is Doppler-shifted with a Doppler factor $\delta = [\Gamma(1 - \beta \cos \theta)]^{-1}$. The electron energy spectrum in the jet-frame follows a broken power-law, with indices p_1 and p_2, and is characterised by a minimum and maximum energy ($E_{\rm min}$, $E_{\rm max}$) and a break energy ($E_{\rm br}$). The power in the SED is mostly influenced by the Doppler factor and both the radius and magnetic field of the emitting region. The shapes of the synchrotron and inverse Compton peaks and the peak frequencies depend strongly on the energies that define the electron population.

Since we only had data in the X-ray and γ-ray regimes, it was impossible to model the entire SED. We therefore added archival radio data, neglecting the observations that only included the core, and infrared data from the NED archive[2]. Assuming that the infrared emission is produced in the same region as the X-rays (the accretion disc or inner jet), we were able to use the column density found in the X-ray spectra, $N_{\rm H} = 9.0 \times 10^{21}$ cm^{-2} to calculate the extinction in the V-band $A_V = N_{\rm H}/(1.79 \times 10^{21}$ cm$^{-2})$ (Predehl & Schmitt 1995). From the extinction in the V-band, we calculated the extinction in the near-infrared bands J, H, and K using the correction factors from Schlegel et al. (1998). We removed the *Suzaku*/XIS data below 1 keV to avoid possible contamination by starburst emission.

Using our best fit of the X-ray spectrum, we were able to constrain some of the parameters. The indices of the power-law are tied to the power-law index of the X-ray spectrum: the first power-law index is $p_1 = 2$ (below $E_{\rm br}$). Starting with this parameter and the initial parameters of the code, we optimised the model. We focused on the energies that characterise the electron population to define the shape of the peaks, and to change the overall energy output in the SED we adjusted the radius of the emitting region and its magnetic field, and the Doppler factor.

We found that the break in the electron power-law is insignificant and we therefore used a single power-law with index $p_1 = p_2$. Furthermore, we found the minimum energy of the electron distribution to be $E_{\rm min} = 5.6 \times 10^6$ eV and the maximum

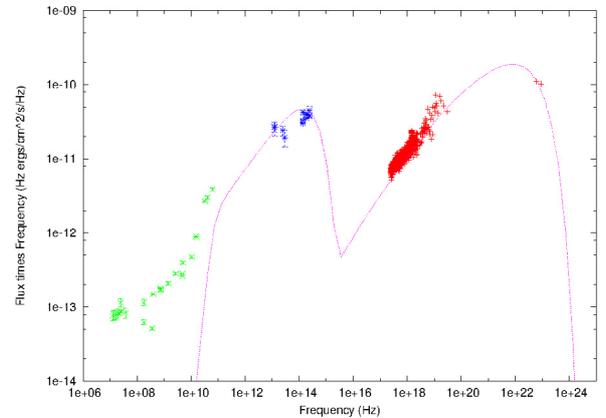---

[2] http://ned.ipac.caltech.edu/

Fig. 3. SED showing 3C 111 unabsorbed fluxes and the SSC one-zone model. Crosses indicate data extracted and analysed in this work. We have added archival and deabsorbed IR and radio points from NED. The line shows the SSC model. See Table 2 for the values used.

energy $E_{\rm max} = 6.8 \times 10^9$ eV. The Doppler factor is $\delta = 14$, the radius of the spherical emission-volume is $R_{\rm s} = 2 \times 10^{16}$ cm, and the magnetic field is $B = 4 \times 10^{-4}$ G. The parameters that we used to fit the data can be found in Table 2, and the resulting plot is presented in Fig. 3. The addition of an external Compton component does not improve the model fit.

4. Discussion

To evaluate the physical processes that dominate the high-energy emission from X-ray to γ-rays in 3C 111, we studied the X-ray spectrum and the broad-band SED.

4.1. X-ray spectrum

We constrained the high-energy cut-off of 3C 111 by applying the `pexrav` model, which describes an exponentially cut-off power-law spectrum reflected from neutral material (Magdziarz & Zdziarski 1995) in XSPEC. We found a cut-off $E_{\rm cut} = 227^{+143}_{-67}$ keV using data from INTEGRAL/ISGRI, *Suzaku*/XIS and PIN, and *Swift*/BAT. An indication of the cut-off can already be seen in the power-law indices of the individual fits, which go from $\Gamma \sim 1.6$ in the soft X-rays to ~ 1.9 in the hard band (Table 1). We also applied the physical `compPS` model to

the same data, which yielded an electron temperature $kT_e = 91^{+22}_{-48}$ keV that can be related to the cut-off energy via $E_{cut} \simeq 3kT_e$. The electron temperature that we found using the `compPS` model is consistent with the cut-off energy that we derived using the `pexrav` model.

The value we found for the high-energy cut-off is consistent with the upper limits reported by Dadina (2007) and Ballo et al. (2011) and the measurement by Molina et al. (2009). Rivers et al. (2011) found, using data from RXTE from 3 keV to ≳100 keV, that the addition of a cut-off does not improve their fit of 3C 111. This might be because we used a combination of different instruments and a wider energy range for the spectrum presented here.

A high-energy cut-off is a typical property of the high-energy spectra of Seyfert galaxies, and the value we derived for 3C 111 is in the expected range for cut-off energies observed in Seyferts (Beckmann et al. 2009; Dadina 2008).

We measured the reflection in 3C 111 using both the `compPS` and the `pexrav` model to be $R = 1.8^{+0.5}_{-0.7}$ and $R = 0.7 \pm 0.3$, respectively. Since these models are very different (`pexrav` is a descriptive model and `compPS` is a physical model), we expect to find different measures of the reflection. Beckmann et al. (2011) applied both models to the hard X-ray spectrum of the radio galaxy Cen A and found that the reflection in the case of `compPS` is also slightly higher though consistent with the reflection found using the `pexrav` model.

The reflection scaling factor we derived, $R = 0.7 \pm 0.3$, using the `pexrav` model can be compared to earlier work using the same model. Our results are consistent with an upper limit reported by Dadina (2007), as well as with the constraints obtained by Molina et al. (2009) and Ballo et al. (2011). The latter also reported a significantly lower result, $R = 0.19^{+0.05}_{-0.04}$, when using only soft X-ray data between 0.4 keV and 10 keV. This is to be expected since the reflection component depends on the energy band used to observe it. In addition Rivers et al. (2011) did not detect a reflection component when applying the `pexrav` model between 3 keV and ≳100 keV. They constrained the model so as to avoid a high-energy cut-off, which might explain the difference from our result.

The value we measured is also consistent with the average Seyfert properties values of $R = 1.2^{+0.6}_{-0.3}$ for Seyfert 1 and $R = 1.1^{+0.7}_{-0.4}$ for Seyfert 2 galaxies (Beckmann et al. 2009).

For the iron line at 6.11 keV, we found that its $EW = 85 \pm 11$ eV, which is similar to the results of Ballo et al. (2011) and Tombesi et al. (2010). Smaller values between $EW > 33$ eV and $EW > 40$ eV were reported by Tombesi et al. (2011). Since the source is variable, it is likely that the iron line EW varies depending on the continuum. Figure 4 shows the correlation between the flux between 4 keV and 10 keV and the EW of the iron line for several observations. The correlation between the flux and the EW has a significance of >95%, a Pearson's test coefficient of $r = -0.3$, and a Spearman's rank correlation coefficient $r_s = -0.7$, showing a believable correlation between the flux level and the EW. When we did not consider the large EW measurement based on RXTE data presented by Rivers et al. (2011), we get a highly significant correlation with a probability of >99%. Tombesi et al. (2010, 2011) also report the power-law indices changing for the different data sets. Similarly, using a different data set, Ballo et al. (2011) derived an $EW = 38^{+11}_{-9}$ eV. Since there is a difference of several months between both data sets this value can again be explained by the source variability.

We found that the EW is smaller than the average value for Seyfert galaxies Dadina (2008), at $EW = 448 \pm 67$ eV, which
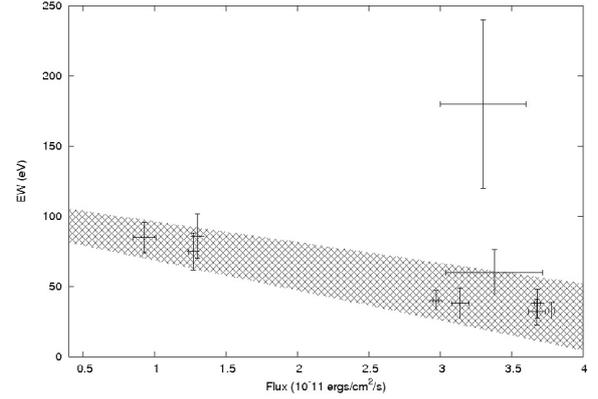

Fig. 4. Flux of the source versus the EW of the iron line. Data taken from Tombesi et al. (2010, 2011), Ballo et al. (2011), Rivers et al. (2011), Lewis et al. (2005), and Eracleous et al. (2000) and this work are plotted as points with error bars. We used a linear regression fit to derive a correlation between the two parameters. The fit is plotted with grey dashed lines indicating the 1σ error region.

can be compared to the average for Seyfert 1 galaxies of $EW = 222 \pm 33$ eV and for Seyfert 2 galaxies of $EW = 693 \pm 195$ eV. The correlation between EW of the iron line and the underlying power-law flux indicates that the line flux does not vary significantly, whereas the continuum varies by a factor of ~5. This can be naturally explained if the majority of the continuum flux is produced in a non-thermal and variable process. The small value of the EW of the iron line may indicate that the X-ray spectrum of 3C 111 does not only contain a thermal, but also a non-thermal contribution.

We also fitted the spectrum with the physical `compPS` model, deriving a temperature for the electron cloud $kT_e = 91^{+22}_{-48}$ keV, a Compton parameter $y = 0.6 \pm 0.1$ (which corresponds to an optical depth of $\tau = 0.8$), and a reflection component $R = 1.8^{+0.5}_{-0.7}$.

NGC 4151 is a well-studied case of a Seyfert core at hard X-rays. Beckmann et al. (2005) fitted the `compPS` model to the spectrum of the Seyfert galaxy NGC 4151 across the range 2–300 keV. They found for the electron plasma temperature $kT_e = 94^{+4}_{-10}$ keV, a reflection component $R = 0.72 \pm 0.14$ and an optical depth of $\tau = 1.3^{+0.13}_{-0.05}$. The hard X-ray spectrum (3–1000 keV) of Centaurus A, which is another nearby γ-ray detected radio galaxy, was also modelled with `compPS` by Beckmann et al. (2011). This yielded an electron plasma temperature of $kT_e = 206 \pm 62$ keV, a Compton parameter $y = 0.42^{+0.09}_{-0.06}$ (which corresponds to an optical depth of $\tau = 0.26$), and a reflection component of $R = 0.12^{+0.09}_{-0.10}$. NGC 4151 is optically thick, whereas both Cen A and 3C 111 are not. The optical thickness of NGC 4151 depends on the flux state and can decrease to $\tau =\sim 0.3-0.6$ in the dim state (Lubiński et al. 2010), when the electron temperature can increase to $T_e \sim 180-230$ keV. The optical depth of 3C 111 is similar to that of the dim state of NGC 4151, but the electron temperature is closer to the electron temperature of the brighter state. The reflection measured in 3C 111 is higher than those found in both NGC 4151 and Cen A.

Chatterjee et al. (2011) concluded that the X-ray spectrum of 3C 111 is of thermal inverse Compton origin, based on a correlation between the optical and X-ray fluxes, as well as a weak optical polarisation and a smaller variance in the optical than X-ray flux on shorter timescales. They concluded that these findings are consistent with a reprocessing model where the X-rays are mostly produced by inverse Compton scattering of thermal optical/UV seed photons from the accretion disc.

The cut-off we measured using the `pexrav` model may have either a thermal or a non-thermal origin. It can be interpreted as a high-energy cut-off measured in Seyfert galaxies. In the case of 3C 111, the cut-off value is also comparable to the typical cut-offs found in Seyfert galaxies. The cut-off observed in the `pexrav` model can also be caused by non-thermal inverse-Compton scattering processes. In this case, the smooth turn-over of the inverse Compton branch towards higher energies appears as a cut-off in the `pexrav` model. While in the thermal inverse-Compton case the cut-off is exponential, the non-thermal spectrum is curved in such a way that γ-ray and VHE emission cannot be excluded. It is impossible to differentiate between an exponential and a simple cut-off in the hard X-rays based on the data at hand, thus both the non-thermal and the thermal interpretations of the curved X-ray spectrum are still valid. The reflection component is a property of Seyfert galaxies and a result of thermal processes. The value of the one we detect is in the typical range for reflection in Seyfert galaxies. The EW of the observed iron line is smaller than expected for Seyfert galaxies and is also variable, implying that the continuum is similarly variable. We therefore suggest that, while the thermal processes in the X-ray band in 3C 111 seem to dominate, we cannot exclude a non-thermal contribution.

4.2. γ-rays

3C 111 was proposed as a counterpart of the γ-ray source 3EG J0416+3650 in the third CGRO/EGRET catalogue, even though it fell outside the 99% probability region (Hartman et al. 1999). A re-analysis of the data (Sguera et al. 2005) concluded that 3EG J0416+3650 is likely associated with 3C 111. There are no other plausible counterparts in the EGRET error region, which is also larger than previously thought because the quoted errors were statistical only and did not take into account the larger systematic errors caused by inaccuracies in the Galactic diffuse model. The EGRET data were re-analysed (Hartman et al. 2008) when it was found that 3EG J0416+3650 is likely the result of the blending of more than one source. One of these components (detected only above 1 GeV) can be associated with 3C 111. Furthermore, 3C 111 was included in the first *Fermi*/LAT source catalogue (Abdo et al. 2010a) with a significance of 4.3σ. In the second *Fermi*/LAT source catalogue, 3C 111 was excluded because the source was no longer significantly detected (Nolan et al. 2012). However, 3C 111 is very likely to be variable (Ackermann et al. 2011) and therefore no longer detectable in the second year. This was also confirmed by Kataoka et al. (2011), who found a significance $>5\sigma$ for 3C 111 using 24 months of *Fermi*/LAT data and by Grandi et al. (2012) who found that the γ-ray emission is not persistent, but flaring and associated with the ejection of bright radio knots.

Since 3C 111 was detected by CGRO/EGRET and *Fermi*/LAT at different epochs, we assumed that the source is a variable γ-ray emitter. We included data from the first *Fermi*/LAT catalogue where the source was detected significantly. Our analysis gives a power-law index similar to that given in the first catalogue with a comparable flux level (Abdo et al. 2010a).

4.3. Spectral energy distribution

To construct the SED of a variable source, simultaneously acquired data are necessary in order to ensure that we make an unbiased measurement. The data used in the SED of 3C 111 were not acquired simultaneously, which can affect the results in the sense that the SED is composed of measurements from different spectral states. This effect is more severe for very variable objects, whereas at most wavebands 3C 111 is moderately variable. We refer, for example to Beckmann et al. (2007) who found no significant variability in hard X-rays for their study of 9 months of *Swift*/BAT data. For the radio domain, Grossberger et al. (2012) present decade-long light curves showing variations of up to a factor of 2 which we can consider as insignificant variability in the context of the SED. For other radio galaxies, it has also been shown that the use of non-simultaneous data to construct the SED does not introduce any significant bias. For example, the radio galaxies NGC 1275 (Antón et al. 2004) and Pictor A (Brown & Adams 2012) were also similarly analysed using time-averaged SEDs. The results for the physical parameters should thus not be significantly affected by the moderate variability of 3C 111.

The archival radio data that we used to model the SED were not well-represented by our SSC model. For observatories that operate at different wavebands, there are large differences in the data acquired in terms of the field of view and resolution. The resolution depends on the wavelength via $RL = \lambda/D$, where RL is the resolution, λ the wavelength, and D the dish diameter. It is therefore possible that we probe different regimes in the broad-band SED, something that the one-zone model does not account for.

In SSC models, the relativistic electron-energy distribution is often assumed to be a broken power-law with a break energy E_{br}, a power-law index before the break of $p_1 < 3$ and a power-law index after the break of $p_2 > 3$ (see for example Ghisellini et al. 1996; Tavecchio et al. 1998; Krawczynski et al. 2004). The electron population is confined to region of radius R_s and a magnetic field B that moves with a Doppler factor δ along the jet. The electrons emit synchrotron radiation and inverse Compton radiation using the synchrotron photons as seed photons. For electrons with energies below the break energy E_{br}, cooling of the electrons is the dominant emission source and in the regime after the break, the escape of electrons from the source dominates. The peak synchrotron power is emitted by electrons at the break energy (Tavecchio et al. 1998). In the case of 3C 111, we found that using a broken power-law gave a break energy of $E_{br} = 1.6$ GeV and power-law indices of $p_1 = 2$ and $p_2 = 2.2$. The break between the two power-laws is insignificant. We therefore applied a single power-law with an index $p = 2$, based on the power-law index of the X-ray spectrum. In the case of a single power-law, the maximum synchrotron power is emitted near the maximum energy of $E_{max} \simeq 7$ GeV.

The energies that define the electron distribution, E_{min} and E_{max} influence the shape of the synchrotron and inverse Compton peak and were chosen by ourselves empirically. If the minimum energy, E_{min}, decreases, the maximum of the peak occurs at lower frequency and the slopes are less steep. Increasing the E_{min} increases the depth between the synchrotron and inverse Compton peak and steepens the rise and fall of the peaks. The maximum energy, E_{max}, is tied to the peak frequencies of both the synchrotron and inverse Compton peak: increasing this value would increase the peak frequencies.

Abdo et al. (2010b) modelled the SED of the core of the radio galaxy Cen A, using simultaneous data from the radio up to the γ-ray regime, applying a single-zone SSC. Comparing the parameters for this model and our own (see Table 2), it is clear that the models have significantly different parameter values. The magnetic field has a much higher value in the case

of Cen A (B = 6.2 G), than the value we found for 3C 111 (B = 0.04 G). The higher magnetic field increases the resulting flux because the synchrotron power depends on the magnetic field. In contrast, the Doppler factor used to model Cen A is low (δ = 1) compared to the value we found for 3C 111, δ = 14. A lower Doppler factor means that the emission is less boosted and therefore appears less energetic. There are also three orders of magnitude difference between the emission volumes: for Cen A, R_s = 3×10^{15} cm was used, whereas we assumed R_s = 2×10^{16} cm for 3C 111. Since this defines the amount of particles this also causes the flux to be lower for Cen A than for 3C 111. The higher value used for the magnetic field is attenuated by the lower Doppler factor and radius for Cen A, which causes the overall output to be lower, as expected for the less luminous source.

Pictor A is another FR-II radio galaxy that was detected by *Fermi*/LAT as reported by Brown & Adams (2012), who modelled the SED of one of the hot-spots in the radio-lobe of Pic A with a one-zone SSC model using the same code that we applied. They concluded that it is impossible to describe both the X-ray and γ-ray emission using the SSC model. Since the γ-ray emission is very variable it is likely to originate from the jet, whereas the X-rays originate from the hot-spot. This appears to indicate that more than one zone is needed to model the entire SED.

Błażejowski et al. (2005) also used the Krawczynski code to model the high-energy peaked BL Lac object Mrk 421, assuming only an SSC component. The parameter values they derived are shown in Table 2. Both the Doppler factor (δ = 10) and the emitting region radius ($R_s = 7 \times 10^{15}$ cm) chosen for Mrk 421 are smaller than those chosen for 3C 111, but are larger than those of Cen A. Similar to Cen A, the magnetic field value for Mrk 421, B = 0.4 G, is a factor of 10 stronger than for 3C 111. The smaller radius and Doppler factor decrease the flux, but owing to the strong magnetic field the flux in the SED for Mrk 421 is higher than the flux of 3C 111.

We conclude that the overall emission from 3C 111 can be modelled with a simple synchrotron self-Compton model, where no additional thermal Compton component is needed. Since the X-rays appear to be (mostly) of thermal origin, the SED provides an upper limit to the non-thermal emission in the X-ray band. There may be a thermal component in the SED, but with the current data we are unable to disentangle the possible thermal component from the overall non-thermal emission.

5. Conclusion

The origin of the high-energy emission from non-blazar AGNs remains unclear. Marscher et al. (2002) suggested that with the acceleration of the inner regions of the accretion disc a shock front will stream along the jet and the expulsion of a superluminal bright knot will follow. Grandi et al. (2012) show, using *Fermi*/LAT data, that the GeV emission of 3C 111 appears to originate from a compact knot confined to within 0.1 pc. This knot is clearly separate from the core and placed 0.3 pc from the central engine.

By analysing the X-ray spectrum and the broad-band SED, we have studied the nature of the high-energy emission of the radio galaxy 3C 111. We have presented an X-ray spectrum between 0.4 keV and 200 keV using data of 3C 111 acquired by several instruments and showed that the best-fit model is an absorbed cut-off power-law with both a reflection component and a Gaussian component to account for the iron line at 6.4 keV. The values we found for the reflection and high-energy cut-off are

similar to those found in Seyfert galaxies, which would indicate that there is a thermal core visible. The cut-off can also originate from non-thermal processes and the EW of the iron line is variable and smaller than expected for Seyfert galaxies. We therefore conclude that the X-ray spectrum is mainly of thermal origin, but there may be a small non-thermal contribution.

Using the X-ray spectrum, together with γ-ray data from *Fermi*/LAT and archival deabsorbed radio and infrared data, we modelled the broad-band SED of 3C 111 using a single-zone synchrotron self-Compton model. This model is non-thermal and we also did not need to include an additional thermal component to model the SED. Since the X-ray emission is likely to have a combined thermal and non-thermal origin, the SSC model we used may overestimate the non-thermal contribution in the X-ray band and should therefore be considered an upper limit.

In conclusion, it seems that the high-energy emission from 3C 111 consists of both thermal and non-thermal components. In the X-ray spectrum, the thermal components manifest themselves in terms of an iron line and reflection. The non-thermal component is visible through the variability in the EW of the iron line. The high-energy cut-off can be the result of either thermal or non-thermal inverse Compton scattering, but our present spectrum does not allow us to distinguish which process is occurring. The broadband SED can be modelled with a non-thermal model, but it is possible there is a thermal component that we are unable to discern with the current data set.

References

Abdo, A. A., Ackermann, M., Ajello, M., et al. 2009, ApJS, 183, 46
Abdo, A. A., Ackermann, M., Ajello, M., et al. 2010a, ApJS, 188, 405
Abdo, A. A., Ackermann, M., Ajello, M., et al. 2010b, ApJ, 719, 1433
Abdo, A. A., Ackermann, M., Ajello, M., et al. 2010c, ApJ, 720, 912
Ackermann, M., Ajello, M., Allafort, A., et al. 2011, ApJ, 743, 171
Antón, S., Browne, I. W. A., Marchã, M. J. M., Bondi, M., & Polatidis, A. 2004, MNRAS, 352, 673
Antonucci, R. 1993, ARA&A, 31, 473
Arnaud, K. A. 1996, in Astronomical Data Analysis Software and Systems V, eds. G. H. Jacoby, & J. Barnes, ASP Conf. Ser., 101, 17
Atwood, W. B., Abdo, A. A., Ackermann, M., et al. 2009, ApJ, 697, 1071
Ballo, L., Braito, V., Reeves, J. N., Sambruna, R. M., & Tombesi, F. 2011, MNRAS, 418, 2367
Barthelmy, S. D., Barbier, L. M., Cummings, J. R., et al. 2005, Space Sci. Rev., 120, 143
Baumgartner, W. H., Tueller, J., Markwardt, C., & Skinner, G. 2010, BAAS, 42, 675
Beckmann, V., Shrader, C. R., Gehrels, N., et al. 2005, ApJ, 634, 939
Beckmann, V., Barthelmy, S. D., Courvoisier, T. J.-L., et al. 2007, A&A, 475, 827
Beckmann, V., Soldi, S., Ricci, C., et al. 2009, A&A, 505, 417
Beckmann, V., Jean, P., Lubiński, P., Soldi, S., & Terrier, R. 2011, A&A, 531, A70
Błażejowski, M., Blaylock, G., Bond, I. H., et al. 2005, ApJ, 630, 130
Bridle, A. H., & Perley, R. A. 1984, ARA&A, 22, 319
Brown, A. M., & Adams, J. 2012, MNRAS, 421, 2303
Chatterjee, R., Marscher, A. P., Jorstad, S. G., et al. 2011, ApJ, 734, 43
Dadina, M. 2007, A&A, 461, 1209
Dadina, M. 2008, A&A, 485, 417
Dermer, C. D., & Schlickeiser, R. 1993, ApJ, 416, 458
Eracleous, M., Sambruna, R., & Mushotzky, R. F. 2000, ApJ, 537, 654
Fanaroff, B. L., & Riley, J. M. 1974, MNRAS, 167, 31

Ghisellini, G., Maraschi, L., & Dondi, L. 1996, A&AS, 120, C503
Grandi, P., Torresi, E., & Stanghellini, C. 2012, ApJ, 751, L3
Grossberger, C., Kadler, M., Wilms, J., et al. 2012, Acta Polytech., 52, 010000
Hartman, R. C., Bertsch, D. L., Bloom, S. D., et al. 1999, ApJS, 123, 79
Hartman, R. C., Kadler, M., & Tueller, J. 2008, ApJ, 688, 852
Jorstad, S. G., Marscher, A. P., Lister, M. L., et al. 2005, AJ, 130, 1418
Kataoka, J., Stawarz, Ł., Takahashi, Y., et al. 2011, ApJ, 740, 29
Koyama, K., Tsunemi, H., Dotani, T., et al. 2007, PASJ, 59, 23
Krawczynski, H., Hughes, S. B., Horan, D., et al. 2004, ApJ, 601, 151
Lebrun, F., Leray, J. P., Lavocat, P., et al. 2003, A&A, 411, L141
Lewis, K. T., Eracleous, M., Gliozzi, M., Sambruna, R. M., & Mushotzky, R. F. 2005, ApJ, 622, 816
Lichti, G. G., Bottacini, E., Ajello, M., et al. 2008, A&A, 486, 721
Linfield, R., & Perley, R. 1984, ApJ, 279, 60
Lubiński, P., Zdziarski, A. A., Walter, R., et al. 2010, MNRAS, 408, 1851
Magdziarz, P., & Zdziarski, A. A. 1995, MNRAS, 273, 837
Maraschi, L., Ghisellini, G., & Celotti, A. 1992, ApJ, 397, L5
Marscher, A. P., Jorstad, S. G., Gómez, J.-L., et al. 2002, Nature, 417, 625
Molina, M., Bassani, L., Malizia, A., et al. 2009, MNRAS, 399, 1293
Nolan, P. L., Abdo, A. A., Ackermann, M., et al. 2012, ApJS, 199, 31
Poutanen, J., & Svensson, R. 1996, ApJ, 470, 249
Predehl, P., & Schmitt, J. H. M. M. 1995, A&A, 293, 889
Rivers, E., Markowitz, A., & Rothschild, R. 2011, ApJS, 193, 3
Sargent, W. L. W. 1977, ApJ, 212, L105
Schlegel, D. J., Finkbeiner, D. P., & Davis, M. 1998, ApJ, 500, 525
Sguera, V., Bassani, L., Malizia, A., et al. 2005, A&A, 430, 107
Takahashi, T., Abe, K., Endo, M., et al. 2007, PASJ, 59, 35
Tavecchio, F., Maraschi, L., & Ghisellini, G. 1998, ApJ, 509, 608
Tombesi, F., Sambruna, R. M., Reeves, J. N., et al. 2010, ApJ, 719, 700
Tombesi, F., Sambruna, R. M., Reeves, J. N., Reynolds, C. S., & Braito, V. 2011, MNRAS, 418, L89
Tueller, J., Baumgartner, W. H., Markwardt, C. B., et al. 2010, ApJS, 186, 378
Urry, C. M., & Padovani, P. 1995, PASP, 107, 803
Winkler, C., Courvoisier, T. J.-L., Di Cocco, G., et al. 2003, A&A, 411, L1